Research Article

ADVANCED
PHOTONICS
NEXUS

Relative timing jitter compression in a Fabry–Pérot cavity-assisted free-running dual-comb interferometry

Chen Liu,[a,b] **Liang Xu,**[a,b] **Lei Zhang,**[c] **Chi Zhang,**[a,b,*] **and Xinliang Zhang**[a,b]
[a]Huazhong University of Science and Technology, Wuhan National Laboratory for Optoelectronics, Wuhan, China
[b]Optics Valley Laboratory, Wuhan, China
[c]Wuhan Vanjee Optoelectronic Technology Co., Ltd., Wuhan, China

Abstract. Dual-comb interferometric systems with high time accuracy have been realized for various applications. The flourishing ultralow noise dual-comb system promotes the measurement and characterization of relative timing jitter, thus improving time accuracy. With optical solutions, introducing an optical reference enables 10^5 harmonics measurements, thereby breaking the limit set by electrical methods; nonlinear processes or spectral interference schemes were also employed to track the relative timing jitter. However, such approaches operating in the time domain either require additional continuous references or impose stringent requirements on the amount of timing jitter. We propose a scheme to correct the relative timing jitter of a free-running dual-comb interferometry assisted by a Fabry–Pérot (F–P) cavity in the frequency domain. With high wavelength thermal stability provided by the F–P cavity, the absolute wavelength deviation in the operating bandwidth is compressed to <0.4 pm, corresponding to a subpicosecond sensitivity of pulse-to-pulse relative timing jitter. Also, Allan deviation of 10^{-10} is obtained under multiple coherent averaging, which lays the foundation for mode-resolved molecular spectroscopic applications. The spectral absorption features of hydrogen cyanide gas molecules at ambient temperature were measured and matched to the HITRAN database. Our scheme promises to provide new ideas on sensitive measurements of relative timing jitter.

Keywords: optical frequency comb; dual-comb interferometry; relative timing jitter; postcalibration; precision optical metrology.

Received Apr. 5, 2024; revised manuscript received Jun. 22, 2024; accepted for publication Jul. 22, 2024; published online Aug. 16, 2024.

[DOI: 10.1117/1.APN.3.5.056014]

1 Introduction

Born from optical frequency comb (OFC) technology,[1–3] the dual-comb system is made up of two OFCs with a slight difference in repetition frequency (f_{rep}) that inherits high stability and frequency accuracy better than 10^{-18} supported by each OFC at optical frequency,[4,5] which promotes the research of optical metrology applications.[6–12] By establishing the mutual coherence between dual combs, the high level of temporal consistency promotes a range of applications, including absolute distance measurement based on time-of-flight methods,[13] remote synchronization as well as calibration between combs,[14] and on-chip clock distribution networks with femtosecond precision,[15] to name a few. Specifically, two sequences of stable ultrashort pulses emitted from two independent OFCs walk off temporally with a fixed interval of $\delta\tau = 1/f_{\mathrm{rep}} - 1/(f_{\mathrm{rep}} + \Delta f_{\mathrm{rep}}) \approx \Delta f_{\mathrm{rep}}/f_{\mathrm{rep}}^2$ from each other, where Δf_{rep} is the offset repetition frequency between two combs, forming the regular asynchronous optical sampling (ASOPS) in the time domain. Such a downsample approach enables optical carrier frequencies that would be difficult to detect directly to be captured by lower-cost, more mature radio-frequency (RF) devices. In such scenarios, the time axis is linearly magnified through the equivalent sampling by, for example, more than 10^5 times. This allows recording the optical signal in real time at the RF domain, providing a powerful tool for measuring ultrafast phenomena within

---

*Address all correspondence to Chi Zhang, chizheung@hust.edu.cn microseconds. In high-precision time-domain applications, such as equivalent time sampling and dual-comb spectroscopy (DCS), the relative timing jitter requires rigorous measurement and subsequent reduction to guarantee a time synchronization between two pulse trains. Typically, a mode-lock fiber laser-based dual-comb ranging system with a timing jitter lower than the subfemtosecond results in a high resolution of the submicrometer.[13] For dual-comb-based spectroscopic applications, Shi et al.'s work[16] numerically derives an amplified spontaneous emissions (ASE) noise-induced quantum-limit relative timing jitter of 0.82 fs to introduce a relative linewidth of 650 Hz into the free-running single cavity DCS and finally set a 65-MHz spectral uncertainty at the measurement.

Timing jitter refers to the degree to which the optical pulse deviates from the perfect periodic position. For mode-locked lasers, the timing jitter was set by the intracavity ASE noise in two ways, given as[17]

$$S_{\Delta t}^{\mathrm{ASE}}(f)=\frac{D_T}{(2\pi f)^2}+\frac{4D^2 f_{\mathrm{rep}}^2 D_\omega}{(2\pi f)^2\cdot[(2\pi f)^2+\tau_{\omega_c}^{-2}]}, \tag{1}$$

where f is the offset frequency, D_T and D_ω are the diffusion coefficients for ASE-induced group delay velocity and center wavelength shift of pulse trains, respectively, D is half the net dispersion of the cavity, and $\tau_{\omega_c}^{-2}$ is the decay time of frequency fluctuations. For the first term in Eq. (1), ASE noise is coupled directly into the timing jitter; the second term is known as the Gordon–Haus jitter, where ASE noise is coupled to the timing jitter through dispersion-affected center frequency fluctuations.[18] Besides the ASE noise-induced timing jitter, another factor lies in the coupling from intensity noise by several mechanisms, including slow saturable absorber, Kramers–Krönig-related phase changes, and other nonlinear processes.[19]

The measurement of relative timing jitter between dual combs can be roughly divided into two approaches: electrical and optical. In electrical schemes, a fast photodetector (PD) is usually used to detect f_{rep} and their higher harmonics $n\cdot f_{\mathrm{rep}}$. Usually $n>100$; then $n\cdot\Delta f_{\mathrm{rep}}$ is obtained by electrical mixing and finally analyzed by commercial signal analyzers.[20] However, the optical signal is limited by the detection speed of the PD and electrical equipment, and the noise characteristics of this electrical reference set an inherent lower boundary for measurement sensitivity to satisfy the demands for phase noise characterization.[21] Excess intensity-phase noise coupling also degrades the measuring accuracy of the noise of interest.[22] Gigahertz bandwidth limitations can be overcome using the optical method, thus achieving $n>10^5$th harmonic measurements. To overcome the bottleneck of electrical approaches, the optical method either bypasses the noise-limited electrical reference or records the traces of relative timing jitter in real time, employing interaction between dual combs, thereby improving the detection sensitivity to the femtosecond level.[16,23–25] For example, nonlinear ASOPS based on a sum-frequency generation process records the relative timing jitter to the idler component, which provides the ability to track the relative timing jitter directly and achieves the measurement capability of the attosecond level by equivalently amplifying the time axis.[16] However, the occurrence of nonlinear processes sets a low threshold for power. In addition, such solutions inherently demand that the deviation of the timing jitter be less than the duration of the pulse. By introducing an optical reference, a multiheterodyne detection method can derive a time-varying function of the offset repetition frequency while maintaining the minimal intensity-phase noise coupling, which can subsequently be analyzed for phase noise or calibrated in postprocessing.[23,24] The uncorrelated relative timing jitter of the free-running dual-comb system is measured to achieve the subattosecond detection sensitivity. Another reference-free solution borrows the idea of spectral interference to ingeniously transfer the undetectable timing jitter at the femtosecond level in the time domain to the frequency domain.[25] To this end, a dispersive Fourier transform (DFT) process[26] was carried out to map the interference patterns containing relative timing jitter back to the time domain with a mapping factor of $2\pi\beta L$, where βL is the group delay dispersion of the system provided by the dispersive fiber.[25] A high-speed PD and oscilloscope finally recorded the real-time optical signal stream. Through digital signal processing, the timing jitter between round trips can be calculated from interferograms (IGMs), and the relative timing jitter of a counterpropagating all-normal dispersion dual-comb fiber laser was measured to verify the scheme's feasibility. In this way, the measurement frame rate is the f_{rep} of the laser, and the detection sensitivity was also increased by 5 times compared to the optical-referenced heterodyne method. However, the accuracy of this method is highly dependent on the dispersion linearity of the DFT process. Specifically, the residual dispersion of the third or higher order makes the frequency-to-time mapping no longer linear, resulting in the distortion of the calculated relative timing jitter. Besides that, spectral interference patterns of fast oscillations in time-domain waveforms must be captured using large-bandwidth detection equipment, while smaller Fourier frequencies also rely on that.

2 Materials and Methods

In this work, we exploit the frequency-time mapping relationship to convert the study of relative timing jitter in the time domain to be performed in the frequency domain, inspired by Ref. 25. The relative timing jitter is reflected as deviations in the RF spectrum for a dual-comb interferometry. In turn, tiny deviations in the spectrum can be used to trace the relative timing jitter periodically. The essential prerequisite for realizing the above time-frequency correspondence is that another degree of freedom, i.e., the relative carrier-envelope offset frequency (Δf_{ceo}) noise penalty is effectively suppressed or calibrated in real time.[27,28] In our previous work,[29] it was demonstrated that a passive phase-shifted fiber Bragg grating (PS-FBG) can be used to calibrate spectral distortions caused by Δf_{ceo} penalties owing to its ultranarrow notch filter bandwidth (~100 MHz). Here, we compare the effect of locking mode on Δf_{rep} under three different operating conditions, i.e., electrical-referenced locking, free-running, and Fabry–Pérot (F–P) cavity-assisted locking, shown in Fig. 1. It should be emphasized that the v axes in Fig. 1 have no real physical meaning. In reality, ASOPS implements pulse-to-pulse sampling of the probe light to the signal light, and the optical carrier signal at the effective time is linearly stretched into a laboratory time to yield the downsampled RF waveform within the Nyquist bandwidth. The corresponding optical frequency can be inverted using upconversion. For the case shown in Fig. 1(a), the reference signal for f_{rep} stabilization is usually provided by a commercial RF reference source, and the degree of stability depends on the reference quartz crystal inside the facility. There is a definite frequency transfer relationship between f_{rep} (megahertz) and

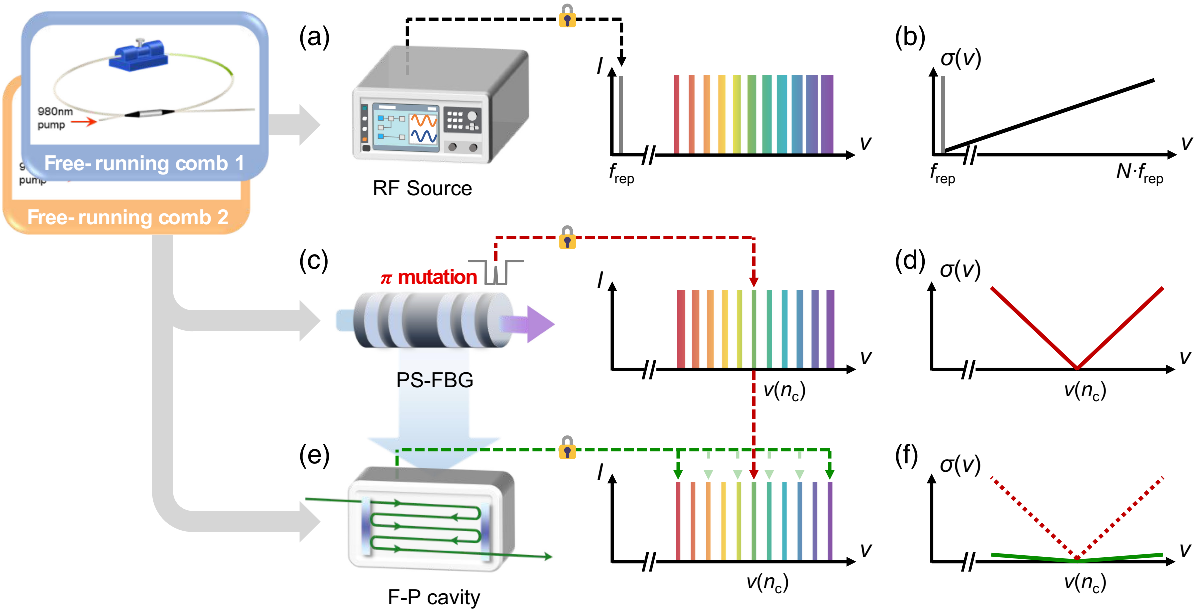

Fig. 1 Principle of the F–P cavity-assisted relative timing jitter locking scheme and comparison of offset repetition rate locking stabilities under three operating conditions. (a) The RF source provides a reference signal to lock f_{rep} directly. (c) Schematic of equivalent locking using a PS-FBG in free-running operation. (e) Schematic of F–P cavity-assisted Δf_{rep} locking in free-running operation. (b), (d), and (f) Schematic representations of the frequency deviation corresponding to the three cases.

the optical comb frequency (terahertz), and the transfer quantity N is usually larger than 10^6.[3] Although f_{rep} is accurately locked in the RF domain, the accumulation of frequency instability [i.e., $\sigma(\nu)$] causes instability in the optical frequency, which significantly deteriorates the accuracy as known by the elastic tape theory[30,31] [Figs. 1(a) and 1(b)].

Figures 1(c) and 1(e) compare the equivalent locking of the Δf_{rep} when OFCs are completely free-running and where neither frequency degree of freedom is interfered with. Specifically, Δf_{rep} jitter leads to telescopic changes in the RF comb lines, while Δf_{ceo} jitter leads to an overall shift in the combs, both of which broaden the combs over long time scales, resulting in degradation of resolution and distortion of the measurements.[27] Using a PS-FBG allows Δf_{ceo} jitter to be tracked in real time,[29,32] setting the stage for subsequent equivalent Δf_{rep} locking. In general, the optical field of the Gaussian pulse trains output by the two mode-locked fiber lasers can be approximated separately as

$$E_{1n}(t) = \sqrt{p_1}\,\exp\left[-2\ln 2\left(\frac{t}{T_{\text{pw}}}\right)^2\right] \cdot \exp[i2\pi(nf_{\text{rep1}} + f_{\text{ceo1}})t + i\Phi_1], \tag{2}$$

$$E_{2m}(t) = \sqrt{p_2}\,\exp\left[-2\ln 2\left(\frac{t - m\delta\tau}{T_{\text{pw}}}\right)^2\right] \cdot \exp[i2\pi(mf_{\text{rep2}} + f_{\text{ceo2}})t + i\Phi_2], \tag{3}$$

where p is the power intensity, T_{pw} denotes the pulse width, Φ denotes the initial phase, and the subscripts 1 and 2 of all of the above items are used to differentiate between OFCs 1 and 2. After passing through the coupler, the two optical fields interfere to generate an IGM train, and the interference signal can be approximated as

$$\begin{aligned} I_s(t) &= |E_1(t) + E_2(t)|^2 \\ &= |E_1(t)|^2 + |E_2(t)|^2 + 2\,\text{Re}[E_1(t) \cdot E_2^*(t)]. \end{aligned} \tag{4}$$

The third term in Eq. (4) is the mutual interference term between each other. Bringing Eqs. (2) and (3) into Eq. (4), the beat frequency signal can be approximated by considering only the beat frequency results between the most neighboring combs,

$$I_s(t) = A(\nu)\exp\left[-\ln 2\left(\frac{n\delta\tau}{T_{\text{pw}}}\right)^2\right] \cdot \exp[i2\pi(n\Delta f_{\text{rep}} - pf_{\text{rep2}} + \Delta f_{\text{ceo}})t + i\Delta\Phi], \tag{5}$$

where $A(v)$ is a slow-varying envelope function. From Eq. (5), the IGM can be seen as a Gaussian-shaped envelope, whose oscillating frequency is the carrier frequency difference between dual combs. PS-FBGs typically have notch filter bandwidths in the order of 100 MHz, which can be indicated by the gray spectral pattern in Fig. 1(c). Thus, the beat frequency of the adjacent neighboring teeth between dual combs can be extracted as a calibration signal expressed as

$$I_c(t) = A[\nu(n_c)] \cdot \exp\left[-\ln 2\left(\frac{n\delta\tau}{T_{\text{pw}}}\right)^2\right] \cdot \exp[i2\pi(n_c\Delta f_{\text{rep}} - pf_{\text{rep2}} + \Delta f_{\text{ceo}})t + i\Delta\Phi], \tag{6}$$

where n_c is the number of comb modes at the notch center of the PS-FBG, and p is a constant. From Eqs. (5) and (6), both contain $\Delta f_{\mathrm{ceo}}(t)$ in the phase term, which can be eliminated by reconstructing the raw IGM, thereby equivalently locking the comb at $v(n_c)$, as indicated by the red arrow in Fig. 1(c). From the frequency domain point of view, this process can be interpreted as "moving" the frequency center to $v(n_c)$. However, the residual timing jitter still leads to a deviation [Figs. 1(c) and 1(d)]. In Fig. 1(d), $\sigma(v)$ shows a V-shaped distribution centered at $v(n_c)$. This is attributed to the accumulation of $\sigma(v)$ on both sides, with $v(n_c)$ as a virtual "fixed point." Next, an F–P cavity is introduced, and two reflecting end surfaces form a standing wave field inside the cavity; only frequency components satisfying certain phase conditions can output, forming resonance peaks near each transmitted wavelength, resulting in discrete comb spectral features.[33] These discretely distributed resonance peaks provide excellent wavelength references, especially when combined with the stable structural features of the F–P cavity. The wavelength deviation at the very edge [dark green arrow in Fig. 1(e)] can be corrected and then transfer the wavelength stability uniformly to each line in the working bandwidth [light green arrow in Fig. 1(e)], equivalent to performing an optical frequency division operation[34–36] on the wavelength axis. In this way, wavelength deviation under free running is effectively eliminated [evolution of the red to green curve in Fig. 1(f)], and the relative timing jitter is significantly compressed. The commonly used oven-controlled crystal oscillator provides 10^{-9} stability and accumulates frequency deviations on the order of millihertz (mHz) when transferred to optical frequencies. A commercially available F–P cavity has a nominal wavelength thermal stability of ±6 pm over a temperature range of $-5°\mathrm{C}$ to $70°\mathrm{C}$. Dividing the above parameters by the conversion factor M of a dual-comb system and the number of teeth N_{line} in the operating bandwidth, one can obtain that each comb line shares a frequency stability of 12 mHz.

As evidenced by the following results, the locking accuracy of the relative timing jitter assisted by the F–P cavity is superior to that of the electrically referenced, thus enabling a free-running DCS. The flowchart of data processing is given, the frequency distribution of the phase calibration signal under free running is calculated, and it is characterized by power spectral densities to show that Δf_{ceo} penalty correction is achieved in both free-running and electrical reference locking cases. Next, the results of the wavelength calibration show that the wavelength accuracy corrected by the calibration is superior to the case of electrical reference, even under free-running cases. The absolute wavelength deviations below 0.4 pm over the entire band correspond to a subpicosecond sensitivity of pulse-to-pulse relative timing jitter. Calculations of the Allan deviation show that a stability of 10^{-10} can be achieved after multiple coherent averaging. Finally, the gas absorption spectra of hydrogen cyanide gas molecules were characterized using the free-running dual-comb interferometry and matched to the HITRAN database, enabling mode-resolved molecular spectroscopy applications.

3 Results

3.1 Experimental Setup

We carried out free-running DCS to demonstrate the superiority of the F–P cavity-assisted scheme compared with the conventional electrical-referenced one. The schematic diagram of the experimental setup is shown in Fig. 2. Two identical homemade erbium-doped mode-locked fiber lasers served as the dual-comb source with a f_{rep} of 100 MHz. The lasers work in the stretched-pulse state by optimizing the intracavity net dispersion to near zero in the negative dispersion region,[37] which helps to reduce the Gordan–Haus jitter as well,[38] according to Eq. (1). The working bandwidth of both combs exceeds 130 nm for broadband spectroscopic applications as shown in Fig. 2(b). The passive fiber devices-aided reference-free postprocessing scheme was organized in Fig. 2(a) to establish the mutual coherence between two OFCs without introducing any bulky negative feedback control mechanisms. Two OFCs with a common path are divided into three paths by a combination of optical couplers (OCs), one of which is used for probing, while the other two perform calibration operations. Among them, one PS-FBG with a 118.3-MHz notch bandwidth measured using a fast-sweeping

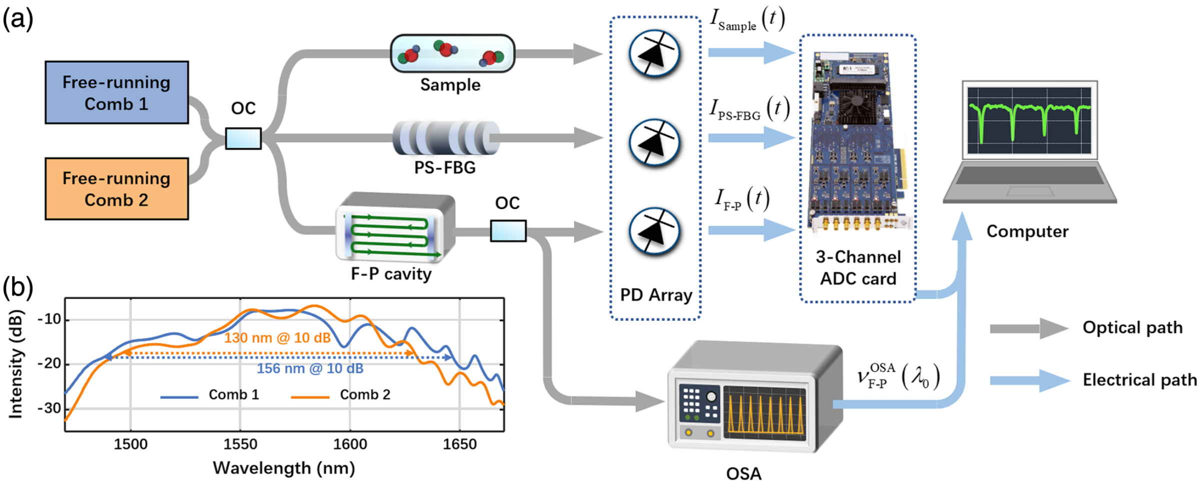

Fig. 2 Schematic diagram of the experimental setup. (a) Two free-running combs pass through the sample, PS-FBG, and F–P cavity synchronously. Three optical streams are captured by a low-speed PD array and recorded through a three-channel ADC card. A commercial OSA is employed to record transmission spectra of the F–P cavity simultaneously. All signals are processed on a computer. (b) Output spectra of the OFCs. OC, optical coupler.

method[29] is set to correct the Δf_{ceo} penalty between dual combs. Although the PS-FBG is a temperature-sensitive device, the core is to filter one line in a dual-comb interferometer. Therefore, even if the temperature change causes a drift of the notch center, the ability does not change and does not lead to a failure of the phase calibration, but only to set a different reference for postprocessing. To reduce the environmental impact, we sealed the PS-FBG in a metal box. Different from other paths, the optical signal passing through the F–P cavity is redivided into two paths, simultaneously recording the transmission spectrum using a commercial optical spectral analyzer (OSA) with a 0.02-nm resolution for followed wavelength calibration. All three optical path signal streams are captured by a low-speed PD array and subsequently received by a three-channel analog-to-digital converter (ADC) card under a 100-MSa/s sampling rate to meet the Nyquist sampling criterion. Because of the symmetry of the setup, the optical path difference among the three signals introduced by passive devices or the sample under test is negligible. In other words, the three signals are temporally consistent. Eventually, four electrical signals (three from ADC and one from OSA) are sent to a computer to perform the calibration procedure to retrieve the spectral absorption characteristics of the sample under test.

The hydrogen cyanide gas cell was chosen as the demonstration. 16-frame synchronous raw data were recorded. Limited by the memory depth of the ADC card, the time window for each frame recorded is 160 ms. After interpolating the measured interference signal, the gravity of the envelope is determined to be the center burst of the IGM.[39] The time difference between two adjacent central bursts in each frame represents the average repetition difference between the IGM and the two adjacent interference cycles, denoted as $\Delta\overline{f}_{\mathrm{rep}}$. The time window of $1/2\Delta\overline{f}_{\mathrm{rep}}$ is extended to both sides around the center burst of each IGM, and it is divided into a single processing unit for the execution of online postprocessing procedures. The individual IGM window split here is not the same as the actual interference period because the repetition difference changes randomly, and the interval determined by the peaks is only the average value.

3.2 Validation of the Postcalibration Algorithm

The block diagram shown in Fig. 3 illustrates the postprocessing process of the raw data. The broadband F–P cavity used for wavelength calibration is considered the sample under test, and the signal detected is $I_{\mathrm{F\text{-}P}}(t)$. As the dual-comb passes through, the comb-like spectrum produces a signature of the periodic bulge near the center burst of each IGM [inset figure in Fig. 3(a)]. Performing a fast Fourier transform (FFT) directly yields a chaotic spectrum in which the RF comb lines are overlapped. This is due to the deterioration of coherence between two combs, which causes the RF comb lines to be broadened and distorted over a long time. Concurrently, the signal detected from the PS-FBG path is recorded as a phase calibration signal and is denoted as $I_{\mathrm{PS\text{-}FBG}}(t)$, presenting a single-frequency signal covering the entire interference period [inset figure in Fig. 3(b)], which suggests its 118.3-MHz notch filtering bandwidth can only filter out a single comb tooth. We performed a Hilbert transform (HT) on two signals to obtain their phases as a function of time as well as their time-varying phase difference, shown in Figs. 3(d) and 3(e), respectively. The effective window for interference to occur is much smaller than the period of the

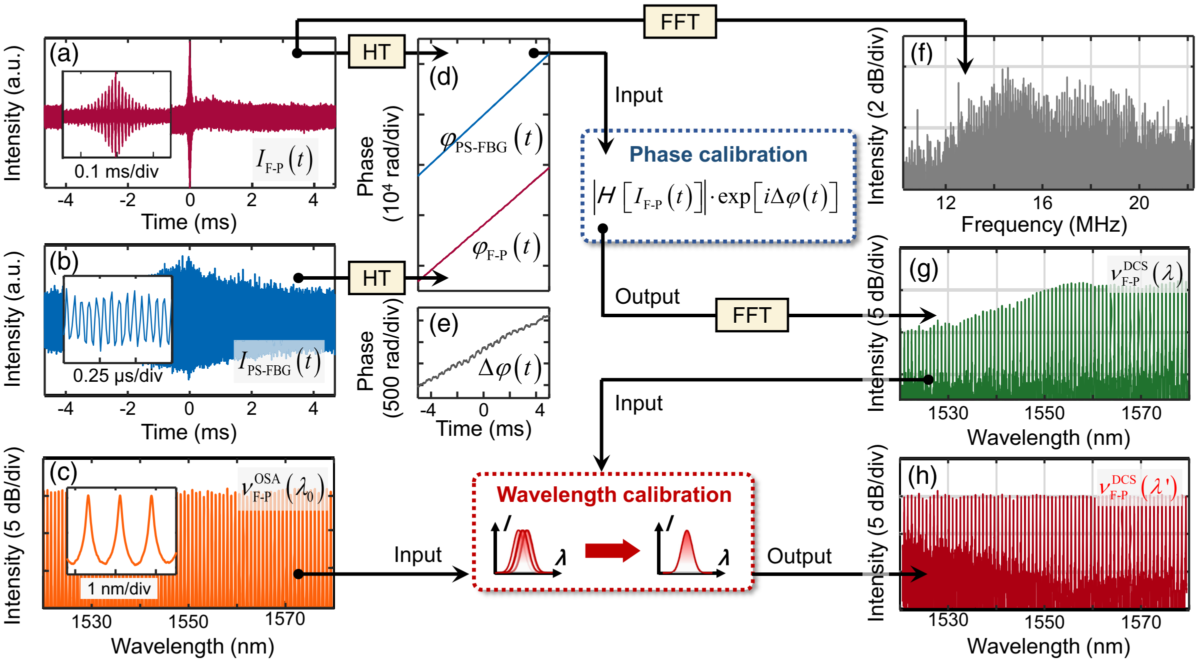

Fig. 3 Block diagram of the online calibration process. Raw data recorded [(a), (b)] by the ADC card and (c) by the OSA. The subscript of the signal indicates the fiber device that passed through. Panels (d) and (e) plot the time-varying phases of (a) and (b) obtained by the HT and their difference, respectively. (f) The raw spectrum of (a) by performing the FFT. (g) Spectrum of the signal after performing phase calibration of (a) using the time-varying phase difference plot in (e). (h) Spectrum after performing wavelength calibration and spectral shaping on (g) taking (c) as the reference.

IGM determined by Δf_{rep}, so the 2π ambiguity can be avoided when unwrapping the phase.[40] As confirmed by Eqs. (4) and (5), the Δf_{ceo} jitter is contained in both time-varying phase signals $\varphi_{\text{F-P}}(t)$ and $\varphi_{\text{PS-FBG}}(t)$. Thus, reconstructing the time-domain signal utilizing the phase difference $\Delta\varphi(t)$ [Fig. 3(e)] can effectively correct the Δf_{ceo} penalty, mathematically expressed as $|H[I_{\text{F-P}}(t)]| \cdot \exp[i\Delta\varphi(t)]$, where H denotes the HT. This operation is known as the phase calibration and the output spectrum $v_{\text{F-P}}^{\text{DCS}}(\lambda)$ after phase calibration is attained by performing FFT on the reconstructed waveform, where the superscript "DCS" indicates the detect facility. As shown in Fig. 3(g), comb-like transmission spectra of F–P cavity features are presented instead of a chaotic one [Fig. 3(f)]. A transmission spectrum with a central wavelength of 1550 nm, a 60-nm bandwidth span, and a 100-GHz free spectral range was obtained. Since both signals [Figs. 3(a) and 3(b)] experience the same fluctuation, this temporal consistency makes phase calibration reliable. However, the retrieved spectra still suffer from wavelength deviations due to residual relative timing jitter. To this end, the spectrum of the F–P cavity $v_{\text{F-P}}^{\text{OSA}}(\lambda)$ measured by the commercial OSA with a 0.02-nm resolution was taken as a wavelength reference [Fig. 3(c)] whose spectral profile was removed by measuring the background spectra simultaneously. Similarly, the superscript "OSA" indicates the detection facility. In this way, wavelength deviations can be eliminated through a resampling process, equivalent to reconstructing the original wavelength axis λ in Fig. 3(g), to a new one, λ'. Meanwhile, the spectral profile in Fig. 3(g) was fitted and reshaped to obtain the normalized absorption spectrum $v_{\text{F-P}}^{\text{DCS}}(\lambda')$ as an output version of the processing. From the vertical comparison of Figs. 3(f)–3(h), the raw, chaotic spectrum is calibrated for the Δf_{ceo} penalty to obtain a secondary intermediate spectrum with a slight wavelength deviation, and the final normalized absorption spectrum is obtained by resampling with the reference spectrum to correct the wavelength deviation caused by the residual relative timing jitter.

The validity of the two calibration processes needs to be further checked under the free-running state. Figure 4 shows the distribution of frequencies extracted from $I_{\text{PS-FBG}}(t)$. We select frames 2, 7, and 10 from the 16-frame signal corresponding to Figs. 4(a)–4(c), respectively. The scatterplots show the corresponding frames' computed $\Delta\bar{f}_{\mathrm{rep}}$ evolution distribution over time. Under free-running operation, the $\Delta\bar{f}_{\mathrm{rep}}$ of the three frames are around 76.85, 165, and 246.9 Hz, respectively. As the $\Delta\bar{f}_{\mathrm{rep}}$ increases, each frame contains more IGM cycles, i.e., each frame corresponds to a denser scattering distribution with the same time window. By performing a short-time Fourier transform operation on the IGMs represented by each point in the scatterplot, the frequency-distributed evolution of $I_{\text{PS-FBG}}(t)$ can be calculated. Figures 4(d)–4(f) show the results of calculating the frequency distributions of the 5th, 15th, and 22nd IGMs in the corresponding frames, respectively. The waveform exhibits a single-frequency oscillation at each time point, consistent with the conclusion that a single-frequency signal was obtained from $I_{\text{PS-FBG}}(t)$, as described in the previous section, and the signal power is concentrated near the center burst (defined in each IGM as the moment $t = 0$) and covers the entire interference period. The single-frequency waveform shows an approximately sinusoidal frequency distribution in all three visual IGMs, which oscillate at about 1 kHz despite different interference periods. This indicates that the Δf_{ceo}-dominated frequency fluctuations vary with time at 1 kHz around their respective fundamental carriers. Besides the main component, it is still possible to observe "power fluctuations" superimposed on a sinusoidal waveform with an oscillatory degree (reflected in rapid frequency changes) much lower than the principal fluctuation. These rapid frequency changes are inferred to be attributed to Δf_{rep} jitter.

For each IGM, the time-varying frequency fluctuations can be used to calculate the power spectral density (PSD) to characterize the noise properties further and quantitatively. We processed all 428 valid IGMs contained in the 16 frames of data. The PSD curves were calculated and then averaged to obtain the expected value (dark curve), accompanied by the error range (light area) in Fig. 5(a). Different IGM periods differ due to

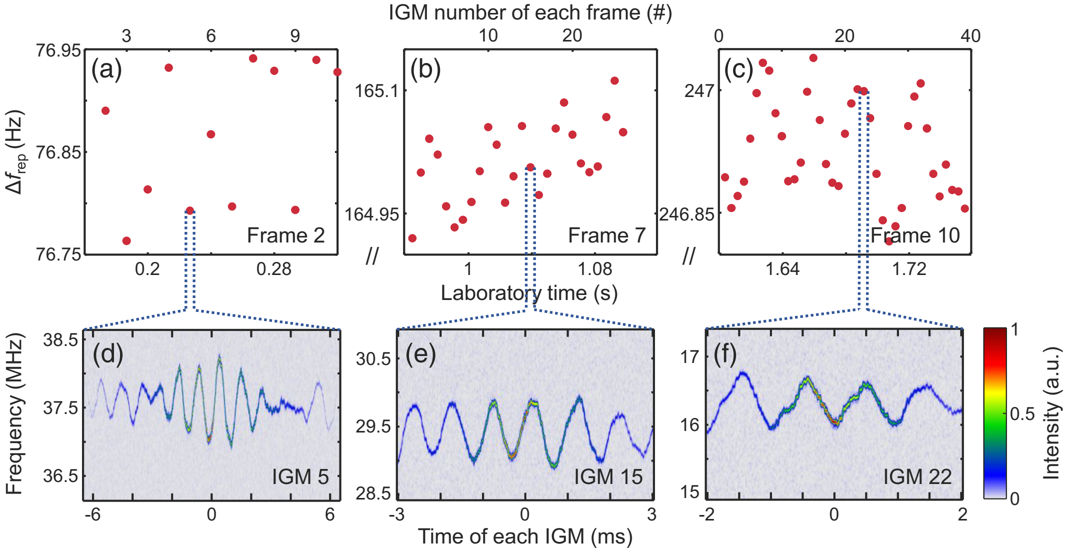

Fig. 4 Distribution of frequencies extracted from $I_{\text{PS-FBG}}(t)$. Calculation of Δf_{rep} evolution over time for (a) frame 2, (b) frame 7, and (c) frame 10 out of 16 frames under free-running operation. (d)–(f) Frequency distributions calculated by each IGM selected from the corresponding frame.

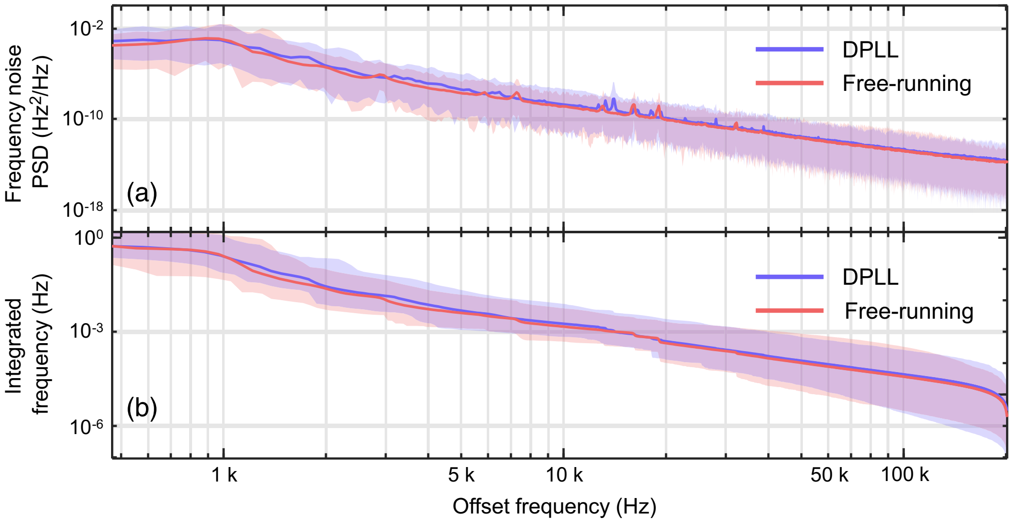

Fig. 5 Comparison of (a) frequency noise PSD curves and (b) integral frequency jitter curves for two operating states calculated from the $I_{\text{PS-FBG}}(t)$.

the free drift of the offset repetition frequency; therefore, the frequency range observed in the calculation of the PSD is different. The offset frequency axes illustrated in Fig. 5(a) are common intervals to extract the common features. The spikes near kilohertz on the PSD curve are broadened due to averaging superposition, which is typically present when focusing on a single IGM's PSD curve. Nevertheless, a bulge of intensity undulation can be observed in the expectation curve around kilohertz, which coincides with the conclusions in Figs. 4(d)–4(f). Next, the PSD curves were used to calculate the integral frequency fluctuations, again obtaining the expectation value and error ranges plotted in Fig. 5(b). For comparison with Δf_{rep} in the electrically referenced case, we used the same methodology to calculate the PSD curves as well as the integral frequency fluctuation curves for the digital phase-locked state named DPLL from Ref. 29, where 430 IGMs were selected and calculated subsequently, as plotted in the purple region in Figs. 5(a) and 5(b). From the calculated PSD and the integrated frequency curves, the Δf_{ceo} of the dual-comb system exhibits similar frequency noise characteristics in both states. In other words, the validity in the free-running state can be guaranteed when performing the phase calibration.

The correction for wavelength deviation through wavelength calibration was then performed and displayed in Fig. 6. The wavelength at the peak position of each resonance peak of the F–P cavity within the operating bandwidth (defined here as 1520 to 1580 nm) was obtained and compared with the reference wavelength measured by the OSA to obtain the absolute wavelength deviation $\sigma(\lambda_p)$, where λ_p is the set of all resonant peak wavelengths. The deviation of all resonance peaks is recorded for fitting to obtain the calibration function, and the original wavelength axis is resampled to obtain the calibrated one, which can be corrected for $\sigma(\lambda_p)$. We compared the $\sigma(\lambda_p)$ for three calibration conditions: electrical reference (i.e., DPLL), free-running, and free-running followed by wavelength calibration. For each IGM, since the wavelength deviation is accumulated uniformly from the center $v(n_c)$ to both sides, the intermediate spare intervals can be approximately described using the calibration function, even though the calibration function is accurate only at the resonance peak wavelength position. A V-shaped distribution is predicted due to the uniform accumulation, as verified by three curves in Fig. 6(a). For the quantitative description of $\sigma(\lambda_p)$, the downconversion factor M of the dual-comb system is required to construct the wavelength axis. In the case of DPLL, Δf_{rep} is locked but inaccurate. When reconfiguring the wavelength axis with a fixed Δf_{rep}, it will inevitably introduce a significant wavelength deviation, especially away from the center. On the other hand, although Δf_{rep} is drifting for the free-running case, it is possible to calculate accurately by determining the interval of the center burst of the IGM with subhertz level [Figs. 4(a)–4(c)]. This is sufficient to restore the wavelength axis more accurately, even though there is a deviation, which leads to the reduction in $\sigma(\lambda_p)$ (orange curve) compared with the DPLL one (cyan curve), as shown in Fig. 6(a). With wavelength calibration, the wavelength deviation is significantly compressed even in free running (magenta curve). Figure 6(b) shows the magnified results of the magenta curve in Fig. 6(a). Statistically, $\sigma(\lambda_p)$ is reduced by about 2 orders of magnitude, and the deviation at all resonance peaks is less than 0.4 pm, which is even lower than the theoretical spectral resolution (0.8 pm). This is meaningful because it sets the sensitivity for measuring the relative timing jitter. Because of the high-frequency fractionation due to the large bandwidth of the F–P cavity, pulse-to-pulse relative timing jitter measurements can be determined with a sensitivity on the subpicosecond level.

In dual-comb applications, simple but effective coherent averaging[41,42] is performed to enhance the signal-to-noise ratio (SNR) of the signal, as the averaging process results in a significant reduction of the Gaussian white noise introduced by the detector. Two representative resonance peaks were chosen, 1520.9 nm away from and 1550.0 nm near the center wavelength, and the Allan variance was calculated under the three calibration conditions, as plotted in Figs. 5(c) and 5(d), represented as triangles and squares, respectively. After multiple coherent averaging, the free-running case exhibits lower deviations than the DPLL case, and the instability of wavelength can be as low as 10^{-10}. For the wavelength calibration, the away-from-center one performs better [last point on the magenta curve in Figs. 5(c) and 5(d)]. This is because the larger the

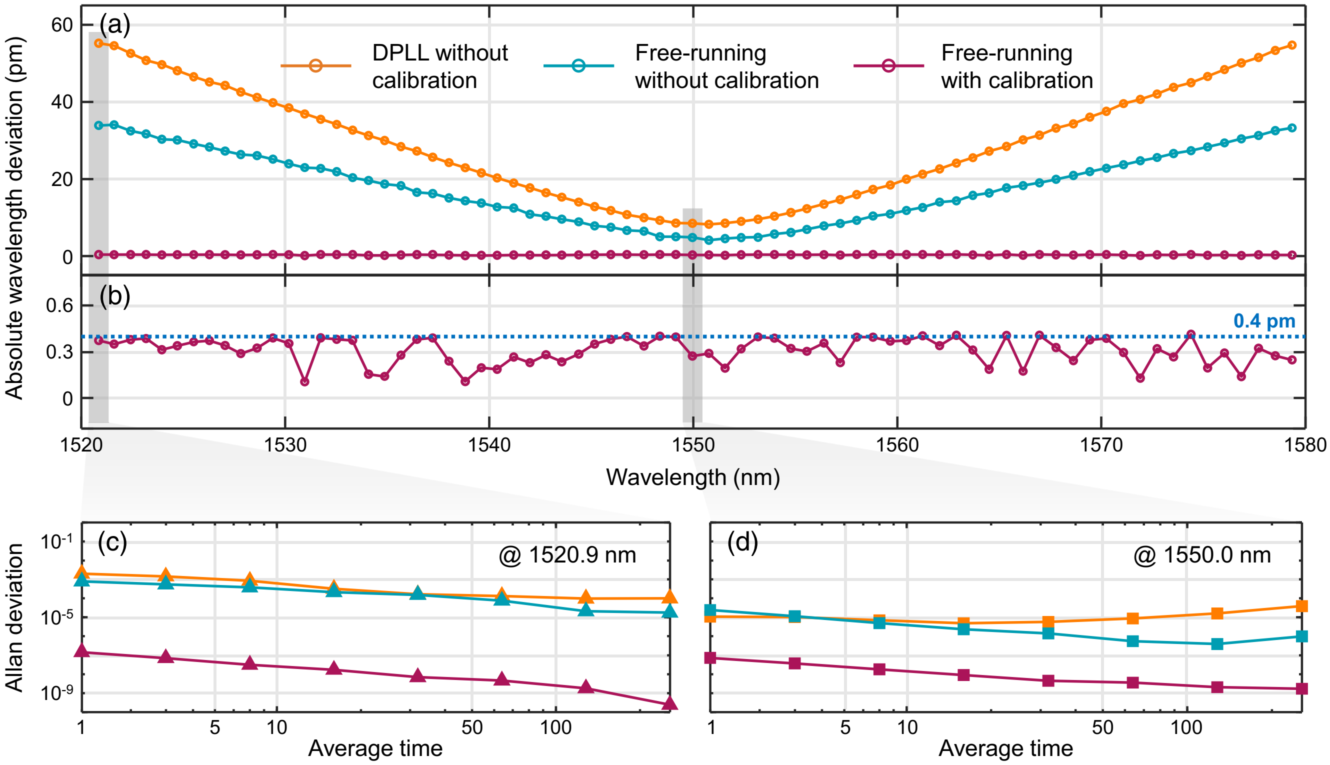

Fig. 6 Characterizations of wavelength calibration results for three operating states. (a) Statistical results of absolute wavelength deviations at the resonance peak of each F–P cavity for the three conditions. (b) Standard deviation after wavelength calibration in free-running operation. (c) and (d) Allan deviations calculated after multiple coherent averaging of the resonance peaks of the F–P cavity 1520.9 nm away from and 1550.0 nm near the center wavelength, respectively.

wavelength deviation, the more accurate the calculation will be when calculating the calibration function. Conversely, when the wavelength deviation is very small, additional fluctuations in the calculated function values occur.

3.3 Gas Molecular Spectroscopy

Using this free-running dual-comb system, we demonstrated the spectral absorption characteristics of hydrogen cyanide ($H^{13}C^{14}N$, 25 Torr, 16.5 cm) gas cell at ambient temperature. The $H^{13}C^{14}N$ molecule has two equally spaced absorption bands, the *P* and *R* branches, near 1.55 μm.[43] Physically, these absorption bands are generated by the multiplicative and combinatorial frequency absorption of low-energy electron leaps, and stretching vibrations of hydrogen-containing atomic groups (N–H bonds and C–H bonds) during the molecule's transition from the ground state to the excited state. A C-band wavelength division multiplexer is inserted in front of the gas cell to be measured and is used to concentrate the optical power in the range of the typical absorption peaks of $H^{13}C^{14}N$.

The results are shown in Fig. 7. All 428 IGMs were postcalibrated and coherently averaged to obtain the absorption spectra, as shown in the red curve in Fig. 7(a), whereas the results without wavelength calibration are marked as light pink curves. As a comparison, we calculated the absorption spectra of $H^{13}C^{14}N$ molecules under the experimental settings from the HITRAN database[44] [dark blue curve in Fig. 7(a)], where the absorption lines are calculated using the standard Voigt profile since the line broadening is affected by both intermolecular collision and the Doppler effect. One should note the significant characteristic asymmetric spectral residue when comparing the HITRAN database from Fig. 7(a), especially in the *R*-branch. Considering the symmetric DCS setup and the high peak power of the pulses, we believe that this deviation is dominated by the nonlinear processes, i.e., self-phase modulation (SPM) and cross-phase modulation (XPM), occurring in the common fiber before passing through the gas sample.[45,46] Specifically, SPM alters each comb's initial spectral baseline, leading to intensity errors in the measurements. At the same time, XPM allows the pulses to attract each other; this arises from the temporally intensity-dependent phase modulation. During ASOPS, this leads to sampling errors in the timing and ultimately results in the unexpected asymmetric spectral residue. An effective solution to weaken the nonlinear penalty is to prechirp two lasers to reduce the peak power before the common fiber.

Figures 7(b) and 7(c) compare the retrieved transmission peaks from the *R* and *P* branches of the $H^{13}C^{14}N$ molecule, both covering the 2.4-nm range. Before wavelength calibration, the deviation appears as a "ghosting" around the true value (corresponding to the HITRAN curve). Here, we show four sets of spectral results without wavelength calibration, two of which show spectral linearity stretching and the other two corresponding to spectral linearity compression, all of which set the PS-FBG's notch center as the "origin." Differences in elastic properties arise from inconsistencies in the pulse misalignment caused by relative timing jitter between dual combs during interference. Specifically, the greater the relative timing jitter, the more pronounced the wavelength deviation is. From the results,

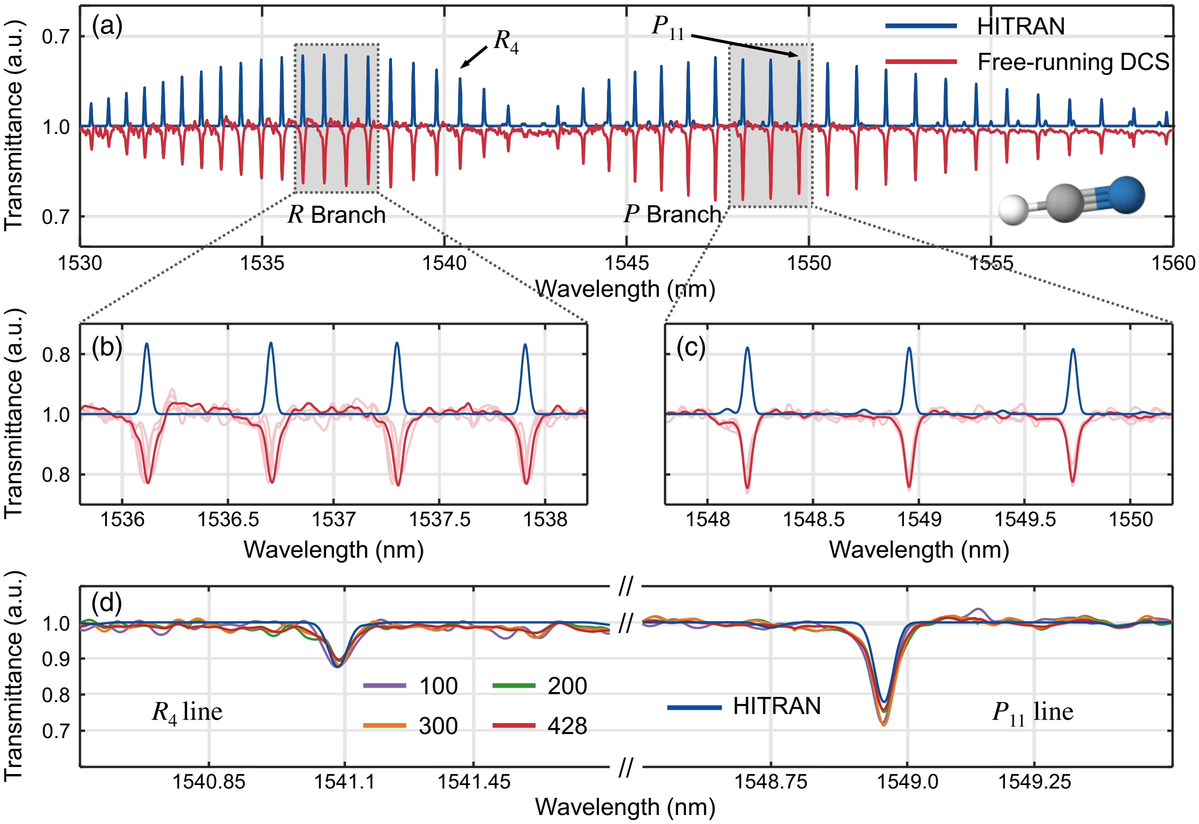

Fig. 7 Spectroscopic measurements of the *P* and *R* branches of the hydrogen cyanide ($H^{13}C^{14}N$) gas absorption cell in free-running operation. (a) Retrieved normalized spectral absorption features of $H^{13}C^{14}N$ compared to the HITRAN database. (b) and (c) Comparison of the difference before and after wavelength calibration in the *R* and *P* branches, respectively. (d) Spectral measurements of the R_4 and P_{11} absorption lines of $H^{13}C^{14}N$ molecules at different averaging times compared to the HITRAN database.

two conclusions need to be explained. First, the *R*-branch is further away from the origin than the *P*-branch, thus accumulating a more significant wavelength deviation in the same data set (conclusion of Fig. 6), whereas the *P*-branch presents more stability. Second, the wavelength dependence of the light source power determines the quality of the retrieved spectra. For our source, the average power in the *R*-branch is about 5 dB lower than that of the *P*-branch [Figs. 2(b) and 3(g)], leading to observed noise undulations between resonance peaks after coherent averaging. That would be effectively suppressed to achieve higher-quality retrieved spectra if dual-comb spectra were preoptimized. The R_4 and P_{11} lines were selected, as shown in Fig. 7(d). The four curves show the spectral measurements performed at 100, 200, 300, and 428 times of coherent averaging, and all show agreement with the HITRAN reference, showing good potential for gas molecular spectroscopy applications.

4 Discussion and Conclusion

We demonstrated a free-running DCS in the Δf_{rep} range of 100 to 300 Hz. However, the range is limited. For DCS applications, the effective spectral information within the optical detection bandwidth is mapped to be detected in the RF domain. Its spectral width can be expressed as $\Delta B = \Delta\nu / M = \Delta\nu \cdot \Delta f_{\mathrm{rep}} / f_{\mathrm{rep}}$, where ΔB and $\Delta\nu$ are the electrical bandwidth and optical frequency bandwidth, respectively. The electrical bandwidth is also limited by Nyquist's law of sampling, i.e., $\Delta B \leq f_{\mathrm{rep}}/2$, and considering that there is a conversion relationship between the optical wavelength bandwidth and the optical frequency bandwidth $\Delta\nu = c \cdot \Delta\lambda / \lambda_0^2$, where c is the speed of light, and λ_0, and $\Delta\lambda$ are the central wavelengths of the light source and the effective bandwidth, respectively. From this, the constrained relationship of the detection frame rate Δf_{rep} can be obtained by

$$\Delta f_{\mathrm{rep}} \leq \frac{f_{\mathrm{rep}}^2 \cdot \lambda_0^2}{2c\Delta\lambda}. \tag{7}$$

For our system, with a λ_0 of 1550 nm and a f_{rep} of 100 MHz, when $\Delta\nu$ reaches 100 nm, the corresponding maximum detection frame rate can be calculated to be 400 Hz without being able to increase it because of the aliasing of the RF spectrum. Using simultaneous in-phase and counter-phase correction to extend the bandwidth to three Nyquist regions without comb lines aliasing,[47] thus breaking the frame rate-bandwidth limit, is expected to increase the detection frame rate even further. In recent years, single-cavity dual-comb technology has flourished,[48,49] perfectly solving the coherence problem of DCS on conventional dual-source platforms, as it produces sources with inherent excellence in inter-coherence without additional frequency locking. It has been realized in dual-wavelength lasers,[50] polarization-multiplexing,[51] directional-multiplexing,[52] and mechanical-sharing[53] scenarios, even in a dual-disk-laser system.[54] Our scheme can be ported to such single-cavity dual-comb systems for higher precision Δf_{rep}-locking, where Δf_{ceo} noise is suppressed by the common mode instead of introducing a phase calibration process.

In summary, we present an F–P cavity-assisted scheme for enhancing relative timing jitter, i.e., Δf_{rep} locking accuracy in a dual-comb system. Due to the excellent wavelength thermal stability of the F–P cavity in the operating bandwidth, i.e. ±0.73 GHz in the range of −5°C to 70°C, the locking accuracy of Δf_{rep} can be further improved. After correcting for Δf_{ceo} penalty in the phase calibration process supported by a PS-FBG with a notch filter bandwidth of 118.3 MHz, the locking accuracy is even better than that of the electrically referenced scheme. Thus, freeform DCS applications are permitted. Careful comparison of the frequency noise PSD curves of the signals from the phase calibration path under both free-running and electrically reference-locked cases shows that there is a similar frequency distribution in both states, thus guaranteeing the validity of performing phase calibration during free running. Next, the validity of the wavelength calibration was also verified under free running, and the locking accuracy of the F–P cavity-assisted scheme was verified to be superior to the electrically referenced scheme. Wavelength deviations below the theoretical optical resolution over the entire operating band allow precision spectroscopic measurements. At the same time, the lower bound of a 0.4-pm deviation provides the scheme with subpicosecond pulse-to-pulse sensitivity in the measurement of relative timing jitter. As a practical spectroscopic measurement application, the spectral absorption characteristics of $H^{13}C^{14}N$ gas molecules were measured at ambient temperature, which showed agreement with the HITRAN database in both the *P* and *R* branches. Our scheme promises new ideas in sensitive measurements of relative timing jitter of dual-comb interferometry and holds the potential to precision metrology applications such as absolute distance measurement, clock synchronization, and high-resolution spectral measurements. Meanwhile, we believe that introducing a broadband F-P cavity to track the wavelength deviation caused by timing jitter with high sensitivity has potential applications in optical sensing and optical network systems with high capacity.

Disclosures

The authors declare no conflicts of interest.

Code and Data Availability

Data underlying the results presented in this paper are not publicly available at this time but may be obtained from the authors upon reasonable request.

Acknowledgments

This work was supported by the National Key Research and Development Program of China (Grant No. 2022YFF0705904) and the National Natural Science Foundation of China (Grant Nos. 61927817 and 62075072).

References

1. J. L. Hall, "Nobel lecture: defining and measuring optical frequencies," *Rev. Mod. Phys.* **78**(4), 1279–1295 (2006).
2. T. Fortier et al., "20 years of developments in optical frequency comb technology and applications," *Commun. Phys.* **2**(1), 153 (2019).
3. S. A. Diddams et al., "Optical frequency combs: coherently uniting the electromagnetic spectrum," *Science* **369**(6501), eaay3676 (2020).
4. H. Leopardi et al., "Single-branch Er:fiber frequency comb for precision optical metrology with 10–18 fractional instability," *Optica* **4**(8), 879–885 (2017).
5. A. Rolland et al., "Ultra-broadband dual-branch optical frequency comb with 10–18 instability," *Optica* **5**(9), 1070–1077 (2018).
6. I. Codington et al., "Dual-comb spectroscopy," *Optica* **3**(4), 414–426 (2016).
7. M. G. Suh et al., "Soliton microcomb range measurement," *Science* **359**(6378), 884–887 (2018).
8. Z. Zhu et al., "Dual-comb ranging," *Engineering* **4**(6), 772–778 (2018).
9. T. Minamikawa et al., "Dual-comb spectroscopic ellipsometry," *Nat. Commun.* **8**, 610 (2017).
10. Q. Wang et al., "Dual-comb photothermal spectroscopy," *Nat. Commun.* **13**, 2181 (2022).
11. A. Asahara et al., "Development of ultrafast time-resolved dual-comb spectroscopy," *APL Photonics* **2**(4), 041301 (2017).
12. J. T. Friedlein et al., "Dual-comb photoacoustic spectroscopy," *Nat. Commun.* **11**, 3152 (2020).
13. I. Coddington et al., "Rapid and precise absolute distance measurements at long range," *Nat. Photonics* **3**, 351–356 (2009).
14. J. D. Deschênes et al., "Synchronization of distant optical clocks at the femtosecond level," *Phys. Rev. X* **6**(2), 021016 (2016).
15. M. Hyun et al., "Femtosecond-precision electronic clock distribution in CMOS chips by injecting frequency comb-extracted photocurrent pulses," *Nat. Commun.* **14**, 2345 (2023).
16. H. Shi et al., "Timing jitter of the dual-comb mode-locked laser: a quantum origin and the ultimate effect on high-speed time- and frequency-domain metrology," *IEEE J. Sel. Top. Quantum Electron.* **24**, 5 (2018).
17. R. Paschotta, "Timing jitter and phase noise of mode-locked fiber lasers," *Opt. Express* **18**(5), 5041–5054 (2010).
18. J. Kim et al., "Ultralow-noise mode-locked fiber lasers and frequency combs: principles, status, and applications," *Adv. Opt. Photonics* **8**(3), 465–540 (2016).
19. R. Paschotta et al., "Optical phase noise and carrier-envelope offset noise of mode-locked lasers," *Appl. Phys. B Lasers Opt.* **82**(2), 265–273 (2006).
20. N. Modsching et al., "High-power dual-comb thin-disk laser oscillator for fast high-resolution spectroscopy," *Opt. Express* **29**(10), 15104–15113 (2021).
21. R. Paschotta et al., "Relative timing jitter measurements with an indirect phase comparison method," *Appl. Phys. B Lasers Opt.* **80**(2), 185–192 (2005).
22. M. J. W. Rodwell et al., "Subpicosecond laser timing stabilization," *IEEE J. Quantum Electron.* **25**(4), 817–827 (1989).
23. S. L. Camenzind et al., "Timing jitter characterization of free-running dual-comb laser with sub-attosecond resolution using optical heterodyne detection," *Opt. Express* **30**(4), 5075–5094 (2022).
24. C. R. Phillips et al., "Coherently averaged dual-comb spectroscopy with a low-noise and high-power free-running gigahertz dual-comb laser," *Opt. Express* **31**(5), 7103–7119 (2023).
25. N. Prakash et al., "Relative timing jitter in a counterpropagating all-normal dispersion dual-comb fiber laser," *Optica* **9**(7), 717–723 (2022).
26. A. Mahjoubfar et al., "Time stretch and its applications," *Nat. Photonics* **11**(6), 341–351 (2017).
27. L. A. Sterczewski et al., "Computational coherent averaging for free-running dual-comb spectroscopy," *Opt. Express* **27**(17), 23875–23893 (2019).

28. J. Roy et al., "Continuous real-time correction and averaging for frequency comb interferometry," *Opt. Express* **20**(20), 21932–21939 (2012).
29. C. Liu et al., "A reference-free dual-comb spectroscopy calibrated by passive devices," *APL Photonics* **8**, 6 (2023).
30. H. R. Telle et al., "Kerr-lens, mode-locked lasers as transfer oscillators for optical frequency measurements," *Appl. Phys. B Lasers Opt.* **74**(1), 1–6 (2002).
31. N. R. Newbury et al., "Low-noise fiber-laser frequency combs [Invited]," *JOSA B* **24**, 1756–1770 (2007).
32. P. Giaccari et al., "Active Fourier-transform spectroscopy combining the direct RF beating of two fiber-based mode-locked lasers with a novel referencing method," *Opt. Express* **16**(6), 4347–4365 (2008).
33. T. Yoshino et al., "Fiber-optic Fabry-Perot interferometer and its sensor applications," *IEEE Trans. Microw. Theory Tech.* **30**, 1612–1621 (1982).
34. T. M. Fortier et al., "Generation of ultrastable microwaves via optical frequency division," *Nat. Photonics* **5**, 425–429 (2011).
35. Y. Yao et al., "Optical frequency divider with division uncertainty at the 10-21 level," *Natl. Sci. Rev.* **3**(4), 463–469 (2016).
36. T. Tetsumoto et al., "Optically referenced 300 GHz millimetre-wave oscillator," *Nat. Photonics* **15**, 516–522 (2021).
37. K. Tamura et al., "Soliton versus nonsoliton operation of fiber ring lasers," *Appl. Phys. Lett.* **64**(2), 149–151 (1994).
38. P. Qin et al., "Reduction of timing jitter and intensity noise in normal-dispersion passively mode-locked fiber lasers by narrow band-pass filtering," *Opt. Express* **22**(23), 28276–28283 (2014).
39. D. Yu et al., "Time-interval measurement with linear optical sampling at the femtosecond level," *Photonics Res.* **11**(12), 2222–2230 (2023).
40. N. B. Hebert et al., "Self-correction limits in dual-comb interferometry," *IEEE J. Quantum Electron.* **55**, 8700311 (2019).
41. I. Coddington et al., "Coherent dual-comb spectroscopy at high signal-to-noise ratio," *Phys. Rev. A - At. Mol. Opt. Phys.* **82**(4), 043817 (2010).
42. G. Ycas et al., "High-coherence mid-infrared dual-comb spectroscopy spanning 2.6 to 5.2 μm," *Nat. Photonics* **12**, 202–208 (2018).
43. G. C. Mellau et al., "Near infrared emission spectrum of HCN," *J. Mol. Spectrosc.* **249**(1), 23–42 (2008).
44. L. S. Rothman et al., "The HITRAN 2004 molecular spectroscopic database," *J. Quant. Spectrosc. Radiat. Transf.* **96**(2), 139–204 (2005).
45. M. Walsh et al., "Pulse interaction induced systematic errors in dual comb spectroscopy," *Opt. Express* **32**, 19837–19853 (2024).
46. G. Agrawal, *Nonlinear Fiber Optics*, Elsevier Science (2019).
47. H. Tian et al., "Quasi-real-time dual-comb spectroscopy with 750-MHz Yb: fiber combs," *Opt. Express* **30**(16), 28427–28437 (2022).
48. C. Zhang et al., "Recent advances and outlook in single-cavity dual comb lasers," *Photonics* **10**(2), 221 (2023).
49. R. Liao et al., "Dual-comb generation from a single laser source: principles and spectroscopic applications towards mid-IR: a review," *J. Phys. Photonics* **2**, 042006 (2020).
50. H. Yoshioka et al., "Dual-wavelength mode-locked Yb: YAG ceramic laser in single cavity," *Opt. Express* **18**(2), 1479–1486 (2010).
51. M. Kowalczyk et al., "Dual-comb femtosecond solid-state laser with inherent polarization-multiplexing," *Laser Photonics Rev.* **15**(8), 1–10 (2021).
52. S. Saito et al., "All-polarization-maintaining Er-doped dual comb fiber laser using single-wall carbon nanotubes," *Opt. Express* **27**(13), 17868–17975 (2019).
53. H. Tian et al., "Dual-comb spectroscopy using free-running mechanical sharing dual-comb fiber lasers," *Appl. Phys. Lett.* **121**, 21 (2022).
54. K. Fritsch et al., "Dual-comb thin-disk oscillator," *Nat. Commun.* **13**(1), 2584 (2020).

Chen Liu received his BS degree in electronic science and technology from Xidian University, Xi'an, China, in 2018. He is currently pursuing his PhD at the Wuhan National Laboratory of Optoelectronics, Huazhong University of Science and Technology (HUST), Wuhan, China. His research interests include optical frequency comb technology, frequency locking of fiber lasers, and precision optical metrology.

Chi Zhang (member, IEEE) received his BS degree in optical information science and technology from HUST, Wuhan, China, in 2009, and his PhD in electrical and electronic engineering from the University of Hong Kong, Hong Kong, China, in 2013. He was a research scientist at the University of Hong Kong. Since 2014, he has been a professor at the Wuhan National Laboratory for Optoelectronics, HUST. He is the author or co-author of more than 100 journal and conference papers. His research interests include nonlinear optics, fiber parametric processes, space-time duality, ultrafast spectroscopy, microscopy, and tomography systems.

Biographies of the other authors are not available.